SIAM J. APPL. MATH.
Vol. 82, No. 3, pp. 950–975

A GRAPHICAL REPRESENTATION OF MEMBRANE FILTRATION*

BINAN GU†, LOU KONDIC†, AND LINDA J. CUMMINGS†

Abstract. We analyze the performance of membrane filters represented by pore networks using two criteria: (1) total volumetric throughput of filtrate over the filter lifetime and (2) accumulated foulant concentration in the filtrate. We first formulate the governing equations of fluid flow on a general network, and we model transport and adsorption of particles (foulants) within the network by imposing an advection equation with a sink term on each pore (edge) as well as conservation of fluid and foulant volumetric flow rates at each pore junction (network vertex). Such a setup yields a system of partial differential equations on the network. We study the influence of three geometric network parameters on filter performance: (1) average number of neighbors of each vertex, (2) initial total void volume of the pore network, and (3) tortuosity of the network. We find that total volumetric throughput depends more strongly on the initial void volume than on average number of neighbors. Tortuosity, however, turns out to be a universal parameter, leading to almost perfect collapse of all results for a variety of different network architectures. In particular, the accumulated foulant concentration in the filtrate shows an exponential decay as tortuosity increases.

Key words. fluid mechanics, filtration, networks, graph theory, discrete calculus

AMS subject classifications. 76S05, 35R02, 94C15, 35E15

DOI. 10.1137/21M1424743

1. Introduction.

In many real membrane filters, cavities in the membrane material (pore junctions) are connected by capillaries or channels (pore throats) of length significantly larger than their radius (see Figure 1). Such slender geometry allows for simplifications of the equations governing filtration. At the same time, the membrane pore structure can be viewed as a complex network with vertices and edges, which represent the pore junctions and pore throats, respectively [14, 21]. A fluid feed with foulants is then driven across the membrane through these channels by the transmembrane pressure, while foulant is deposited on the pore walls.

There is a broad range of studies involving dynamics on networks, such as models of the cardiovascular network [3], chemical reaction networks [23] and optimal control in networks of pipes and canals [6], among many others. Accordingly, there are various graph models that may be used to represent complex networks, including pore networks in porous media. One such setup is the random geometric graph (RGG) model that has garnered significant attention from theoreticians [16, 7], as well as from applied scientists working on applications such as sensor networks [8], social science [24, 12, 25, 2], neuroscience [15], and, most relevant to our work, filtration modeling [22, 10]. The RGG setup involves generating a specified number of random points, uniformly distributed within a specified domain, and then connecting any pair of points that are closer than some search radius (according to the chosen metric).

Within the specific RGG setup used by Griffiths et al. [10] for filtration modeling, the chosen domain is a unit cube (normalized on the membrane thickness and representing a portion of the filter membrane); the metric is the usual three-dimensional

*Received by the editors June 8, 2021; accepted for publication (in revised form) January 19, 2022; published electronically May 31, 2022.
https://doi.org/10.1137/21M1424743
Funding: This work was supported by NSF grant DMS-1615719.

†Department of Mathematical Sciences, New Jersey Institute of Technology, Newark, NJ 07102 USA (bg263@njit.edu, https://web.njit.edu/~bg263/, kondic@njit.edu, linda.cummings@njit.edu).

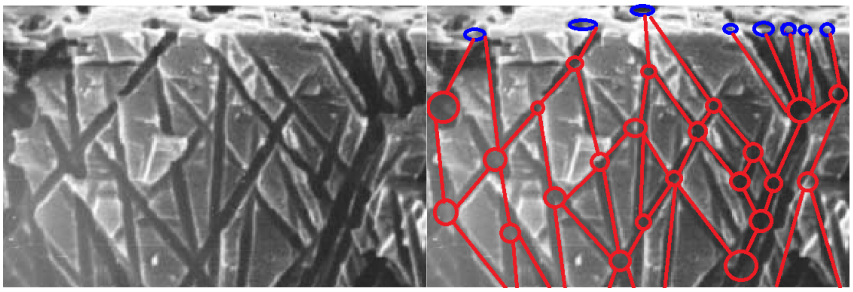

(a) Experimental Image (b) Inlets and Interior Junctions

FIG. 1. *Schematic:* (a) *an experimental image with lateral view of a filter cross section* [1]*;* (b) *a corresponding (partial) graph representation with inlets on the top surface (blue) and interior pore junctions and throats (red).*

(3D) Euclidean distance; and to model top inlets and bottom outlets (see Figure 1(a)) random points are uniformly distributed on the top and the bottom surfaces of the cube. This setup requires four parameters: the number of interior points, the search radius, the number of top inlets, and the number of bottom outlets. Furthermore, the fluid flow is modeled by the Hagen–Poiseuille equations, whose validity relies on the physical assumption that the edges have a small aspect ratio (radius versus length), prompting an additional constraint on the network generation.

Another important aspect of modeling the dynamics of filtration on the membrane network is fouling. Membrane fouling occurs when contaminants transported by the fluid feed within the pore network become trapped within it. There are three primary fouling mechanisms in membrane filtration: (1) adsorption, (2) sieving, and (3) cake layer formation. Adsorption occurs when small particulate foulants are deposited on the pore walls due to physical or chemical interactions with membrane material (or with existing particle deposits). Sieving involves fouling particles of size comparable to the pore size that may partially cover or completely block upstream pore entries or internal junctions. Cake formation occurs during the later stages of filtration, where fouling particles are packed against each other inside the pore throats or on top of the membrane surface, further restricting fluid flow.

In this work, we consider adsorptive fouling only, modeling two main features. First, the fouling particles (referred to simply as particles henceforth) deposit on pore walls as they are advected by fluid flow, thereby reducing foulant concentration in the feed as it traverses the network. Second, pore radius decreases due to the particle deposition on the pore wall. Within a continuum model for the particle concentration, the first effect can be captured by an appropriate sink term in the advection equation for the particle concentration, while the second may be modeled by an evolution equation for the pore radius.

Classical models of particle advective transport on graphs were developed and studied by Chapman and Mesbahi [4], but these authors did not incorporate a sink term to capture external effects such as fouling. Meanwhile, Gu et al. [11] considered a coarse discretization of a transport equation with deposition on regular layered pore structures with interconnections, which can be generalized to more complex networks (represented by graphs). In this work, we combine these two approaches and formulate a transport equation on the network using the graph theoretical framework.

Our principal contributions are to develop and solve a fluid flow and fouling problem on a graph representing the pore network within a membrane filter, by constructing the associated operators based on the underlying graph, and to use our model to identify important correlations between measurable network properties and key filtration performance metrics. The novel random graph generation technique we use achieves two primary goals: the constructed network is such that physical assumptions for the Hagen–Poiseuille fluid flow model remain valid, and the overall number of model parameters is minimized. Our model is described in detail in section 2: in subsection 2.1, we introduce the aspects of graph theory relevant to the present problem; in subsection 2.2 we present a specific graph construction that represents a membrane network; and in subsection 2.3, we describe the fluid flow in an arbitrary pore (edge of the graph), before defining the necessary graph operators and associated function spaces on graphs in subsection 2.4. With these building blocks we are then able to set up the governing equations for fluid flow and foulant transport on a graph in subsections 2.5 and 2.6, respectively. In subsection 2.7, we define the metrics that will be used to characterize filter performance. In section 3 we introduce appropriate scalings to nondimensionalize the model and in section 4 we outline the algorithm we use to solve it. Section 5 contains our results, presented in the context of the performance metrics defined in subsection 2.7. In section 6 we discuss our findings and summarize conclusions.

2. Modeling.

In this section, we describe and construct a graph that models a membrane filter pore network, and set up the governing equations of fluid flow and foulant transport through the network. We then introduce the performance measures associated with our membrane filter, which we will use to characterize filtration effectiveness. We refer the reader to Table 1 for all notation used in this paper.

2.1. Graph theoretical setup.

We consider a membrane filter as a slab of porous material that consists of an upstream (top) surface containing pore inlets, a downstream (bottom) surface containing pore outlets, and a porous interior comprising membrane material as the solid region and pore junctions and throats as the void region. We restrict our attention to a cubic subregion of the membrane slab in which the top and bottom surfaces are squares with side length W separated by distance W (the membrane depth). The pore throats in the interior of this subregion are assumed to be circular cylinders connected at pore junctions, forming a network. We model this interior network of pores by a graph G consisting of a set of vertices V (the pore junctions) and edges E (the pore throats; see Figure 1), more compactly written as

TABLE 1
Key nomenclature used throughout this work.

v_i	ith vertex	e_{ij}	An edge connecting vertices v_i and v_j
V	Set of all vertices	E	Set of all edges
V_{top}	Set of vertices on the top membrane surface	V_{bot}	Set of vertices at the bottom membrane surface
$\mathbf{L_W}$	(Weighted) Graph Laplacian of G	$\mathbf{W}$	Weighted adjacency matrix of G
$\mathbf{M}$	Incidence matrix of G	$\mathbf{M}^{\mathrm{T}}$	Incidence matrix transpose
$\boldsymbol{P}(v_i)$	Pressure at the vertex v_i	$\boldsymbol{C}_i$	Concentration in vertex v_i (unit of number per volume)
P_0	Pressure at membrane top surface	C_0	Foulant concentration in the feed solution
$\mathbf{K}_{ij}$	Conductance of edge e_{ij}	$\mathbf{Q}_{ij}$	Flux through edge e_{ij}
R_{ij}	Radius of edge e_{ij}	A_{ij}	Length of edge e_{ij}
W	Side length of the square cross section	$\chi(\cdot,\cdot)$	Metric on V
D	Search radius	N_{total}	Total number of vertices
$D_{\min}$	Minimal edge length	τ	Tortuosity
μ	Fluid viscosity	α	Parameter related to particle volume
Λ	Affinity between the foulant and the pore wall (unit of velocity)	N	Average number of neighbors for a graph G
H	Throughput	C_{acm}	Accumulated foulant concentration at membrane outlet

$G = (V, E)$. The set of vertices V consists of pore inlets on the membrane top (upstream) surface, pore junctions in the interior of the membrane material where edges (pores) meet, and pore outlets at the downstream surface of the filter. Each edge $e \in E$ represents a pore throat that connects two vertices. From a fluid dynamics perspective the graph forms a flow network, with fluid flowing along the edges and through the vertices. Each edge of the graph is associated with a weight to be specified depending on the context; in our model the weights are associated with the fluid flux through the edge. In constructing G we begin with an undirected graph, with directionality to be imparted by the direction of fluid flow (once defined).

Each vertex $v \in V$ is associated with a Euclidean position vector $\boldsymbol{X}(v) = (X_1(v), X_2(v), X_3(v)) \in \mathbb{R}^3$, where coordinates X_1, X_2 lie in the plane of the membrane, while X_3 is measured perpendicular to the membrane in the direction of flow.

DEFINITION 2.1 (vertex set). *Let $X_3(v)$ be the depth of the vertex v, measured by the shortest distance from the vertex to the membrane inlet surface. Let $V_{\text{top}}, V_{\text{bot}} \subset V$ be the set of vertices that lie in the top and bottom membrane surfaces, respectively,*

$$V_{\text{top}} = \{v \in V : X_3(v) = 0\}, \quad V_{\text{bot}} = \{v \in V : X_3(v) = W\},$$

where W is the depth of the membrane. The set of vertices in the interior of the membrane is given by $V_{\text{int}} = V \setminus (V_{\text{top}} \cup V_{\text{bot}})$.

We further assume that the graph is simple, i.e., no vertex is connected to itself, equivalent to the assumption that fluid always flows out of a pore junction.

DEFINITION 2.2. *An edge $e_{ij} \in E \subseteq V \times V$ is a pair (v_i, v_j), with $i \neq j$ whose existence is governed by a connection law (to be described). We do not distinguish between the order of the pair, namely, $e_{ij} = e_{ji}$.*

2.2. Graph generation for a membrane network. Here we describe a random graph model in the specific context of membrane filtration by clarifying the constituents of V_{top}, V_{bot}, V_{int}, and E, using a variant of the RGG.

In the interior of a rectangular box Ω with square cross sections of side length W and height $2W$, $\Omega := [0, W] \times [0, W] \times \left[-\frac{W}{2}, \frac{3W}{2}\right]$, we generate independent uniformly distributed random points in each cartesian coordinate, from which our set of vertices will be taken. To set up a connection rule for vertices in order to define edges, we first introduce a physically motivated assumption. Earlier work such as that of Iritani [13] and Siddiqui, Arif, and Bashmal [19] suggests that pore throats in certain types of membrane filters are approximately cylindrical and slender, with $R_{ij}/A_{ij} \ll 1$, where R_{ij} and A_{ij} are the radius and length, respectively, of the edge (pore throat) e_{ij} connecting vertices (pore junctions) v_i and v_j. We assume our model membrane filter to be of this type, justifying the use of the Hagen–Poiseuille framework [17] to model steady laminar flow of fluid, assumed to be Newtonian with viscosity μ, within each edge (details of the flow model are in subsection 2.5). In all simulations we present, the initial edge radii are the same for all i, j (though they will shrink at different rates under subsequent fouling depending on local particle concentration), thus validity of the Hagen–Poiseuille model requires that the length of each edge must exceed a certain threshold, $D_{\min}$. Meanwhile, to tune vertex connectivity, we prescribe a parameter D as the maximum possible edge length. More precisely, we define the edge set,

$$E = \{(v, w) \in V \times V : D_{\min} < \chi(v, w) < D\}, \tag{2.1}$$

where $\chi(\cdot, \cdot)$ is the metric on our graph. In this paper, we investigate and compare two distinct metrics: (1) Ω is treated as an isolated domain, with no pores entering

or leaving through the four sides parallel to the X_3 direction, representing an isolated subunit of the whole membrane (*isolated* case), and (2) Ω is treated as a periodic domain such that any pore exiting through one of these four sides reenters on the opposite side (*periodic* case). In each of these two cases the metric is defined by

(2.2)
$$\chi(v,w) = \begin{cases} \|\boldsymbol{X}(v) - \boldsymbol{X}(w)\|_2, & \text{isolated,} \\ \min_{\boldsymbol{z}} \left\| \boldsymbol{X}(v) - \boldsymbol{X}(w) - (\boldsymbol{z},0) \mid \boldsymbol{z} = \{-W,0,W\}^2 \right\|_2, \ D \le \frac{W}{2}, & \text{periodic,} \end{cases}$$

where we note that the periodic metric wraps points around the boundaries in the X_1 and X_2 directions. This metric effectively determines the pore lengths $A_{ij} = \chi(v_i, v_j)$. All scenarios considered in this paper have search radius $D \le \frac{W}{2}$, so we avoid the complication of having pores connect to each other twice (in the periodic case).

To generate the set of upstream (top) inlets V_{top} and downstream (bottom) outlets V_{bot}, we cut Ω with two horizontal planes, $X_3 = 0$ (upstream cutting plane) and $X_3 = W$ (downstream cutting plane). The points of intersection of these planes and the edges defined by (2.1) form the set of pore inlets V_{top} and outlets V_{bot}, respectively (see Figure 2). All points between the planes $X_3 = 0, W$ form the set of interior vertices V_{int}. This cutting procedure effectively eliminates two parameters (number of inlets and outlets) from the RGG setup proposed by Griffiths et al. [10]. We also impose two geometric constraints: (1) total volume of the edges generated by the above scheme cannot exceed that of the box and (2) total cross-sectional area of all inlets (resp., outlets) cannot exceed the area of the top (resp., bottom) membrane surface.

Our setup ensures that vertices in the top and bottom membrane surfaces are not connected by any edges that lie in the same surface. Another nice feature of our graph generation is that top inlets and bottom outlets are always connected to

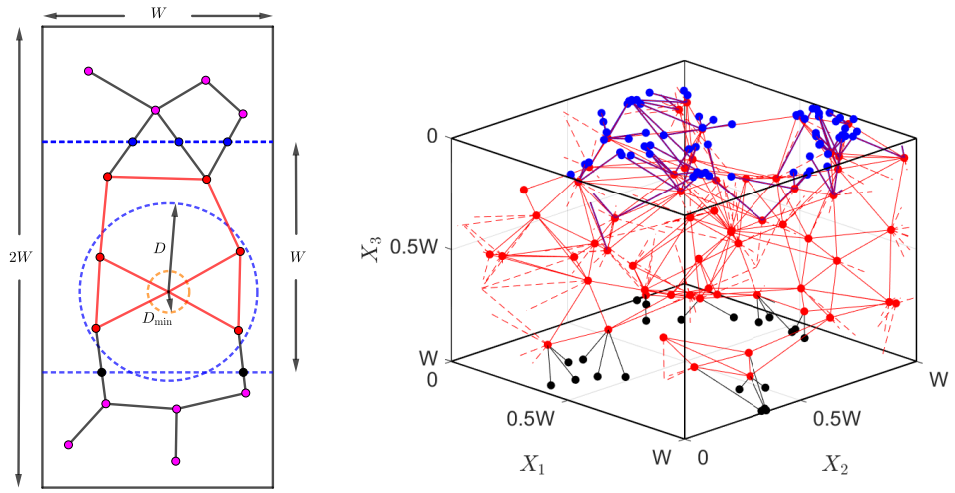

(a) 2D schematic of the 3D graph generation

(b) 3D realization with the periodic metric

FIG. 2. *Labels for* (a) *and* (b)*: red filled circles form* V_{int}*, blue filled circles form induced inlets* V_{top}*, and black filled circles form induced outlets* V_{bot}*. In* (a)*, blue dotted lines are cutting lines (planes in three dimensions), and magenta circles are discarded points. The blue and orange dotted circles form the search annulus enforced by* D *and* $D_{\min}$*. In* (b)*, periodicity is enforced only through the four interior walls per* (2.2)*.*

interior points, a feature that the classical RGG setup does not guarantee (some inlets or outlets may be isolated with positive probability and must be regenerated).

2.3. Flow in an edge. We now briefly describe how Newtonian fluid of viscosity μ flows through a single edge (pore), before introducing the definitions of the relevant graph operators and associated function spaces (in subsection 2.4), necessary to describe flow through the whole network. Two key physical quantities specify the flow: pressure $\boldsymbol{P}(v_i)$ at each vertex $v_i \in V$ and flux $\mathbf{Q}_{ij}$ through each edge $(v_i, v_j) \in E$. For each such edge, with length A_{ij} and radius R_{ij} (assumed to depend only on i, j and time T in the following, but see the more detailed discussion in subsection 2.6), we use the Hagen–Poiseuille equation to describe fluid flow through it. This law gives fluid flux $\mathbf{Q}_{ij}$ in (v_i, v_j) as

$$\mathbf{Q}_{ij} = \mathbf{K}_{ij}\left(\boldsymbol{P}(v_i) - \boldsymbol{P}(v_j)\right), \quad (v_i, v_j) \in E, \tag{2.3}$$

where $\mathbf{K}_{ij}$ are the entries of a weight matrix $\mathbf{K}$ listing the *conductance* of each edge,

$$\mathbf{K}_{ij} = \begin{cases} \frac{\pi R_{ij}^4}{8\mu A_{ij}}, & (v_i, v_j) \in E, \\ 0 & \text{otherwise.} \end{cases} \tag{2.4}$$

Note that $\mathbf{Q}_{ij}$ is spatially uniform within the edge under the Hagen–Poiseuille framework. Moreover, to ensure the Hagen–Poiseuille approximation remains valid we require that the aspect ratio of each edge, R_{ij}/A_{ij}, is small, enforced by choosing $D_{\min}$ (introduced in (2.1)) sufficiently large that

$$\frac{R_{ij}}{A_{ij}} \leq \frac{\max\limits_{(v_i,v_j)\in E} R_{ij}}{D_{\min}} \ll 1.$$

To solve (2.3) on a graph with many edges we must utilize the graph structure to express, for example, the pressure difference $\boldsymbol{P}(v_i) - \boldsymbol{P}(v_j)$ in (2.3), while maintaining flux conservation at each vertex. We introduce the necessary operators below.

2.4. Operators and function spaces on graphs. We now introduce the function spaces and operators required to solve for the above-defined flow on our graph. First, define the set of *vertex functions*

$$\mathcal{V} = \left\{ \boldsymbol{u} : V \to \mathbb{R} : \sum_{x \in V} \boldsymbol{u}(x)^2 < \infty \right\}, \tag{2.5}$$

endowed with inner product $(\boldsymbol{u} \cdot \boldsymbol{v})_{\mathcal{V}} = \sum_{x \in V} \boldsymbol{u}(x)\,\boldsymbol{v}(x)$, and the set of *edge functions*

$$\mathcal{E} = \left\{ \boldsymbol{F} : E \to \mathbb{R} : \frac{1}{2} \sum_{x,y \in V} w_{xy} \boldsymbol{F}(x,y)^2 < \infty \right\}, \tag{2.6}$$

where $\boldsymbol{F}$ is a skew-symmetric function that satisfies

$$\boldsymbol{F}(x,y) = -\boldsymbol{F}(y,x), \tag{2.7}$$

also known as the *flow condition*, and w_{xy} are specified weights. This space is endowed with weighted inner product

$$(\boldsymbol{F}_1 \cdot \boldsymbol{F}_2)_{\mathcal{E}} = \frac{1}{2} \sum_{x,y \in V} w_{xy} \boldsymbol{F}_1(x,y)\, \boldsymbol{F}_2(x,y).$$

An example of a vertex function in the context of our problem is the pressure at each pore junction, while flux is an edge function when a well-defined weight is specified.

We next introduce the incidence matrix (and its transpose), a matrix operator that encodes the most fundamental information of a network represented by a graph—an array specifying the vertices that each edge connects. Its operation on edge functions provides a finite difference of quantities prescribed at connected vertices.

DEFINITION 2.3 (incidence matrix and transpose). *Let $G = (V, E)$ be a graph. The incidence matrix $\mathbf{M}$ is a linear operator $\mathbf{M} : \mathcal{V} \to \mathcal{E}$ such that for $\boldsymbol{u} \in \mathcal{V}$,*

$$(\mathbf{M}\boldsymbol{u})(v_i, v_j) = \boldsymbol{u}(v_i) - \boldsymbol{u}(v_j), \quad v_i, v_j \in V. \tag{2.8}$$

The transpose $\mathbf{M}^{\mathrm{T}} : \mathcal{E} \to \mathcal{V}$ is also a linear operator that satisfies

$$(\mathbf{M}\boldsymbol{u} \cdot \boldsymbol{F})_{\mathcal{E}} = \left(\boldsymbol{u} \cdot \mathbf{M}^{\mathrm{T}}\boldsymbol{F}\right)_{\mathcal{V}}, \quad \boldsymbol{u} \in \mathcal{V}, \quad \boldsymbol{F} \in \mathcal{E}. \tag{2.9}$$

A direct calculation of (2.9) using the above definitions yields the identity

$$\left(\mathbf{M}^{\mathrm{T}}\boldsymbol{F}\right)(x) = \sum_{y:(x,y)\in E} w_{xy}\boldsymbol{F}(x, y), \tag{2.10}$$

which computes a weighted sum of the edge functions whose edges connect to x.

Moreover, each graph G can be associated with a graph Laplacian $\mathbf{L}$, an item central to graph analysis.

DEFINITION 2.4 (graph Laplacian). *The $\mathbf{W}$-weighted graph Laplacian is given by*

$$\mathbf{L}_{\mathbf{W}} := \mathbf{D} - \mathbf{W}, \tag{2.11}$$

where $\mathbf{D}$ is the (diagonal) $\mathbf{W}$-weighted degree matrix for G, with entries

$$\mathbf{D}_{ij} = \begin{cases} \sum_{k=1}^{|V|} \mathbf{W}_{ik}, & j = i, \\ 0 & \text{otherwise}, \end{cases} \tag{2.12}$$

and $\mathbf{W}$ is a weighted adjacency matrix, with nonnegative entries $\mathbf{W}_{ij}$ when $(v_i, v_j) \in E$, to be specified according to context. We also say that e_{ij} is an edge connecting v_i and v_j iff $\mathbf{W}_{ij} > 0$ (or simply, v_i and v_j are connected or adjacent).

$\mathbf{L}_{\mathbf{W}}$ is symmetric since $\mathbf{W}$ is, and the nonzero entries in the diagonal matrix $\mathbf{D}$ represent the respective row sums of $\mathbf{W}$. An unweighted version of $\mathbf{L}_{\mathbf{W}}$ corresponds to the case where $\mathbf{W}_{ij} = 1$ for every $e_{ij} \in E$, and thus each entry of the adjacency matrix is an indicator that identifies an edge between a pair of vertices. In this case, each diagonal element of $\mathbf{D}$ is the number of edges connected to each vertex.

Combining (2.8), (2.10), and (2.11) we obtain the classical result connecting the incidence matrix and the graph Laplacian.

PROPOSITION 2.5. *For $\boldsymbol{u} \in \mathcal{V}$, $\mathbf{M}^{\mathrm{T}}\mathbf{M}\boldsymbol{u} = \mathbf{L}_{\mathbf{W}}\boldsymbol{u}$.*

This result (a proof of which is given by Grady [9]) provides the basis for theoretical understanding of the structure of $\mathbf{M}$ and, in turn, $\mathbf{L}_{\mathbf{W}}$. The continuum analogue of this result is the equivalence between the divergence of a gradient and the Laplacian.

In many applications, the choice of weights $\mathbf{W}$ depends on the physical problem of interest. In the context of membrane filtration it is natural to consider weights such as conductance and flux, which we describe in subsection 2.5 in more detail. We will apply Proposition 2.5 to set up the flow problem on our graph G.

2.5. Flow on a graph. In this section, we outline a general approach to describe fluid flow on a graph using the definitions given in subsection 2.4. We set up the system of governing equations using the structural information of G, i.e., the graph Laplacian $\mathbf{L_W}$ with a properly chosen weight matrix $\mathbf{W}$.

First, we rewrite (2.3) using the incidence operator (2.8),

$$\mathbf{Q}_{ij} = \mathbf{K}_{ij}\left(\boldsymbol{P}\left(v_i\right) - \boldsymbol{P}\left(v_j\right)\right) = \mathbf{K}_{ij}\left(\mathbf{M}\boldsymbol{P}\right)\left(v_i, v_j\right), \quad \left(v_i, v_j\right) \in E, \tag{2.13}$$

where $\mathbf{K}_{ij}$ is given by (2.4). The values of the pressure at the vertices, $\boldsymbol{P}\left(v_i\right)$ for each $v_i \in V$, form a vector of length $|V|$ (a *vertex function*, $\boldsymbol{P} \in \mathcal{V}$). The flux values $\mathbf{Q}_{ij}$ naturally form a matrix. Note that $\mathbf{Q}$ is an *edge function*, $\mathbf{Q} \in \mathcal{E}$, since it satisfies the flow condition (2.7). Next, we impose conservation of flux at each junction,

$$\sum_{v_j:\left(v_i,v_j\right)\in E} \mathbf{Q}_{ij} = 0, \quad v_i \in V_{\text{int}}. \tag{2.14}$$

Using (2.10) with $\boldsymbol{F} = \mathbf{M}\boldsymbol{P}$, using (2.13), and noting that $\mathbf{Q} \in \mathcal{E}$, we obtain for $v_i \in V_{\text{int}}$,

$$0 = \sum_{v_j:\left(v_i,v_j\right)\in E} \mathbf{Q}_{ij} = \sum_{v_j:\left(v_i,v_j\right)\in E} \mathbf{K}_{ij}\left(\mathbf{M}\boldsymbol{P}\right)\left(v_i, v_j\right) = \left(\mathbf{M}^{\mathrm{T}}\mathbf{M}\boldsymbol{P}\right)\left(v_i\right) = \left(\mathbf{L_K}\boldsymbol{P}\right)\left(v_i\right), \tag{2.15}$$

to which we append the boundary conditions

$$\boldsymbol{P}\left(v\right) = P_0, \quad v \in V_{\text{top}}; \quad \boldsymbol{P}\left(v\right) = 0, \quad v \in V_{\text{bot}}, \tag{2.16}$$

modeling the transmembrane pressure difference that drives fluid flow.

Once we solve the linear system (2.15)–(2.16) for pressure $\boldsymbol{P}$, we use (2.13) to compute the entries of the flux matrix $\mathbf{Q}$.

2.6. Foulant advection and adsorptive fouling. The previous section was concerned solely with the flow of Newtonian fluid through the graph. Here we address the fact that in filtration the fluid is a feed solution carrying particles, which are removed by the filter, leading to fouling. Fouling can occur via a number of distinct modes; we consider only adsorptive fouling by particles much smaller than pores, which are transported through the network by the flow and deposit on pore walls.

We use a continuum model for the particle (foulant) concentration within the feed. To characterize particle transport on a network, we must describe the transport on each edge, accomplished via an advection equation with an adsorptive sink [18, 11], then impose conservation of particle flux at each vertex. For each edge $e_{ij} = \left(v_i, v_j\right)$ of length A_{ij}, with Y a local coordinate measuring distance along the edge from v_i (positive in the direction of flux $\mathbf{Q}_{ij}$), let $C_{ij}\left(Y, T\right)$ be the particle concentration at any point of the edge at time T, then

$$\mathbf{Q}_{ij}\frac{\partial C_{ij}}{\partial Y} = -\Lambda R_{ij} C_{ij}, \quad 0 \le Y \le A_{ij}, \tag{2.17a}$$

$$C_{ij}\left(0, T\right) = \boldsymbol{C}_i\left(T\right), \quad \left(v_i, v_j\right) \in E, \tag{2.17b}$$

where Λ is a parameter (with dimensions of velocity) that captures the affinity between the foulant and the pore wall. In practice this could change depending on whether the pore wall is clean or already fouled by particle deposits; in this work we assume Λ

is constant throughout the filtration. We denote by $\boldsymbol{C}_i(T)$ the foulant concentration at the vertex v_i, which acts as a boundary condition for the foulant concentration C_{ij} flowing to downstream edges. The array of $\boldsymbol{C}_i(T)$ values forms a vertex function $\boldsymbol{C}$. For $v_i \in V_{\text{top}}$, $\boldsymbol{C}_i(T)$ is prescribed by imposing a constant boundary condition (the concentration C_0 in the feed solution), and conservation of particle flux is imposed to determine the $\boldsymbol{C}_i(T)$ for $v_i \in V \backslash V_{\text{top}}$.

The system (2.17a), (2.17b) is simple, but once coupled to an evolution equation for pore radii $R_{ij}(Y,T)$ and solved on many different (large) graph realizations to obtain reliable statistics, it is time-consuming to solve numerically. We therefore adopt a convenient approximation (discussed further below), assuming that pore radius does not change appreciably along individual pores, and may thus be considered approximately independent of the coordinate Y. With this assumption, we observe that the system (2.17a), (2.17b) has the analytical solution

$$C_{ij}(Y,T) = \boldsymbol{C}_i(T) \exp\left(-\frac{\Lambda R_{ij}(T)}{\mathbf{Q}_{ij}} Y\right), \quad 0 \le Y \le A_{ij}. \tag{2.18}$$

We write $\tilde{C}_{ij}(T) := C_{ij}(A_{ij}, T)$ to represent the foulant concentration flowing from v_i into an adjacent vertex v_j. Define

$$\mathbf{B}_{ij}(T) := \exp\left(-\frac{\Lambda R_{ij}(T) A_{ij}}{\mathbf{Q}_{ij}}\right), \tag{2.19}$$

as the multiplicative factor by which foulant concentration changes over the length A_{ij} of the edge. By conservation of particle flux at each vertex v_i (suppressing the temporal and spatial dependence for simplicity of notation),

$$\begin{aligned} 0 &= -\overbrace{\sum_{v_k:(v_i,v_k)\in E} \mathbf{Q}_{ik}\boldsymbol{C}_i}^{\text{outgoing}} + \overbrace{\sum_{v_k:(v_i,v_k)\in E} \mathbf{Q}_{ki}\tilde{C}_{ki}}^{\text{incoming}}, \quad v_i \in V\backslash V_{\text{top}}, \\ &= -\boldsymbol{C}_i \sum_{v_k:(v_i,v_k)\in E} \mathbf{Q}_{ik} + \sum_{v_k:(v_i,v_k)\in E} \mathbf{Q}_{ki}\tilde{C}_{ki}, \end{aligned} \tag{2.20}$$

$$= -\boldsymbol{C}_i \sum_{v_k:(v_i,v_k)\in E} \mathbf{Q}_{ki} + \sum_{v_k:(v_i,v_k)\in E} \mathbf{Q}_{ki}\mathbf{B}_{ki}\boldsymbol{C}_k, \tag{2.21}$$

$$\boldsymbol{C}_i(T) = C_0, \quad v_i \in V_{\text{top}}, \quad \forall T \ge 0, \tag{2.22}$$

where C_0 is the constant foulant concentration in the feed solution. Note the conservation of flux used here to derive (2.21) follows a revised definition of the flux matrix $\mathbf{Q}$ (see (B.1) in Appendix B). The first term in (2.20) accounts for all outgoing particle flux from vertex v_i, the second for all incoming flux. Conservation of flux at each $v_i \in V\backslash V_{\text{top}}$ and the definition of $\tilde{C}_{ij}$ are applied in (2.21), which can be written more compactly using $\mathbf{Q}$ as a weight matrix and the in-degree weighted graph Laplacian $\mathbf{L}^{\text{in}}_{\mathbf{Q}} : l^2(V\backslash V_{\text{top}}) \to l^2(V\backslash V_{\text{top}})$,

$$\mathbf{L}^{\text{in}}_{\mathbf{Q}} := \mathbf{D}_{\mathbf{Q}^{\mathrm{T}}} - (\mathbf{Q} \circ \mathbf{B})^{\mathrm{T}}, \tag{2.23}$$

where $\circ$ is the Hadamard product (elementwise matrix product). This operator is similar to (2.11) but with a notion of directionality imparted by $\mathbf{Q}$ (also discussed by Chapman and Mesbahi [4]). The term $\mathbf{D}_{\mathbf{Q}^{\mathrm{T}}}$ is a $\mathbf{Q}^{\mathrm{T}}$-weighted degree matrix (per (2.12)) that accounts for total incoming (upstream) flux of v_i (thereby "in-degree").

The last term, which contributes to the off-diagonal entries of $\mathbf{L}_{\mathbf{Q}}^{\text{in}}$, displays the incoming flux reduced (multiplicatively) by the foulant deposition effect reflected in $\mathbf{B}$. Altogether, the transport equation for foulant concentration can be concisely written as

$$\mathbf{L}_{\mathbf{Q}}^{\text{in}}\boldsymbol{C} = (\mathbf{Q} \circ \mathbf{B})^{\mathrm{T}} \boldsymbol{C}_0, \quad \boldsymbol{C} \in l^2\left(V \backslash V_{\text{top}}\right) \quad \forall T \geq 0, \tag{2.24}$$

$$\boldsymbol{C}_0\left(T\right) = \left(C_0, \ldots, C_0, 0, \ldots, 0\right)^{\mathrm{T}}, \tag{2.25}$$

with boundary condition C_0 specified for each $v \in V_{\text{top}}$ (the number of nonzero entries C_0 in $\boldsymbol{C}_0$ is equal to $|V_{\text{top}}|$, per (2.22)). By solving this linear system, we obtain the particle concentration $\boldsymbol{C}_i$ at each vertex $v_i \in V \backslash V_{\text{top}}$.

We assume that the pore radius shrinkage due to adsorption follows a simple model (used by Sanaei and Cummings [18], among others) such that its rate of change is proportional to local particle concentration. With the approximation introduced above, that pore radius R_{ij} varies only modestly with distance Y along the pore, we assume that its rate of shrinkage is determined by the foulant concentration at the upstream[1] vertex v_i,

$$\frac{dR_{ij}}{dT} = -\Lambda\alpha\boldsymbol{C}_i, \quad R_{ij}\left(0\right) = R_{ij,0}, \quad \left(v_i, v_j\right) \in E, \tag{2.26}$$

where α relates to foulant particle volume; see Appendix A. We also assume that all radii initially take the same value, i.e., $R_{ij,0} = R_0$. This final equation (2.26) closes the membrane filtration model with adsorption.

Our assumption that pore radius is spatially uniform is motivated by significant computational cost savings; we have verified that the simulations reported later in the manuscript are more than 100 times faster compared to those where this simplification is not used. The price to pay for this saving is a slight overestimate of the membrane resistance, and therefore an underestimate of the total throughput. To confirm that the approximation introduced by the model has only a minor influence, we have directly compared a subset of results obtained using this model with results obtained using the full model that allows $R_{ij}(Y, T)$, finding that the difference in throughput is on average around 10% at maximum (and much smaller than 10% where the maximum pore radius D is small compared to the membrane thickness W). The differences in computed values of the particle concentration are smaller still. We consider that this is reasonable, in particular since the approximation allows us to perform efficiently a large number of simulations and explore the influence of variability of results with respect to the model parameters of interest.

In simulating filtration through a network we impose a *stopping criterion* that membrane filtration ends when there exist no flow paths between any vertices in V_{top} and V_{bot}, due to pore closures (individually characterized by $R_{ij} = 0$). The criterion is checked by a pathfinding algorithm. We terminate the filtration at the earliest time T_{final} that the criterion is satisfied. Note that in physical membranes, even when adsorptive foulants have accumulated to the extent that the pore is essentially closed, leakage through the pore may still take place; we have not included such effects in the present model.

2.7. Measures of performance. Volumetric throughput of a membrane filter over its operational lifetime is a commonly used measure of overall efficiency.

[1]This concentration is chosen because it will dictate, in practice, the fastest shrinkage rate at the upstream end of the pore, and pore resistance is dominated by the narrowest pore radius.

DEFINITION 2.6. *The volumetric throughput $V(T)$ through the filter is defined by*

$$H(T) = \int_0^T Q_{\text{out}}(T')\, dT', \quad Q_{\text{out}}(T) = \sum_{v_j \in V_{\text{bot}}} \sum_{v_i:(v_i,v_j)\in E} \mathbf{Q}_{ij}(T),$$

where $Q_{\text{out}}(T)$ is the total flux exiting the filter.

In particular, we are interested in $H_{\text{final}} := H(T_{\text{final}})$, the total volume of filtrate processed by the filter over its lifetime.

Another performance measure is the accumulated foulant concentration in the filtrate, which captures the aggregate particle capture efficiency of the filter.

DEFINITION 2.7. *The accumulated foulant concentration is defined by*

$$C_{\text{acm}}(T) = \frac{\int_0^T C_{\text{out}}(T')\, Q_{\text{out}}(T')\, dT'}{\int_0^T Q_{\text{out}}(T')\, dT'},$$

where

$$C_{\text{out}}(T) = \frac{\sum_{v_j \in V_{\text{bot}}} \sum_{v_i:(v_i,v_j)\in E} \boldsymbol{C}_j(T)\, \mathbf{Q}_{ij}(T)}{Q_{\text{out}}(T)}.$$

Of particular interest is $C_{\text{acm}}(T_{\text{final}})$, which provides a measure of the aggregate particle capture efficiency of the filter over its lifetime.

3. Nondimensionalization. We nondimensionalize the model presented in section 2 with the following scales:

$$\begin{gathered}
\boldsymbol{P} = P_0 \boldsymbol{p}, \qquad \boldsymbol{X} = W\boldsymbol{x}, \qquad A_{ij} = W a_{ij}, \\
(D, D_{\min}) = W(d, d_{\min}), \qquad R_{ij} = W r_{ij}, \qquad R_0 = W r_0, \\
\mathbf{Q}_{ij} = \frac{\pi W^3 P_0}{8\mu} \mathbf{q}_{ij}, \qquad \mathbf{K}_{ij} = \frac{\pi W^3}{8\mu} \mathbf{k}_{ij}, \qquad \mathbf{k}_{ij} = \frac{r_{ij}^4}{a_{ij}}, \\
\boldsymbol{C} = C_0 \boldsymbol{c}, \qquad Y = Wy, \qquad \Lambda = \frac{\pi W P_0}{8\mu}\lambda, \qquad T = \frac{W}{\Lambda \alpha C_0} t, \qquad V = \frac{W^3}{\alpha C_0} v.
\end{gathered} \tag{3.1}$$

Under these scalings we derive dimensionless equations for pressure $\boldsymbol{p}$ and flux $\mathbf{q}$,

$$\mathbf{L}_{\mathbf{k}} \boldsymbol{p} = 0, \tag{3.2a}$$

$$\boldsymbol{p}(v) = 1 \quad \forall v \in V_{\text{top}}; \quad \boldsymbol{p}(v) = 0 \quad \forall v \in V_{\text{bot}}, \tag{3.2b}$$

$$\mathbf{q}_{ij} = \mathbf{k}_{ij} \left(\boldsymbol{p}(v_i) - \boldsymbol{p}(v_j)\right) \quad \forall (v_i, v_j) \in E, \tag{3.2c}$$

where $\mathbf{L}_{\mathbf{k}}$ is defined in (2.11); for foulant concentration $\boldsymbol{c}$,

$$\mathbf{L}_{\mathbf{q}}^{\text{in}} \boldsymbol{c} = (\mathbf{q} \circ \mathbf{b})^{\mathrm{T}} \boldsymbol{c}_0, \quad \mathbf{L}_{\mathbf{q}}^{\text{in}} = \mathbf{D}_{\mathbf{q}^{\mathrm{T}}} - (\mathbf{q} \circ \mathbf{b})^{\mathrm{T}}, \quad \boldsymbol{c} \in l^2(V \backslash V_{\text{top}}), \tag{3.3a}$$

$$\boldsymbol{c}_0 = (1, \ldots, 1, 0, \ldots, 0)^{\mathrm{T}}, \quad \mathbf{b}_{ij} = \exp\left(\frac{-\lambda r_{ij} a_{ij}}{\mathbf{q}_{ij}}\right), \tag{3.3b}$$

where $\mathbf{L}_{\mathbf{q}}^{\text{in}}$ is given by (2.23); and for pore radius r_{ij} (for the pore $e_{ij} = (v_i, v_j)$),

$$\frac{dr_{ij}}{dt} = -\boldsymbol{c}_i, \quad r_{ij}(0) = r_0, \quad \forall (v_i, v_j) \in E. \tag{3.4}$$

The dimensionless throughput is given by

$$h(t) = \frac{1}{\lambda}\int_0^t q_{\text{out}}(t')\,dt', \quad q_{\text{out}}(t) = \sum_{v_j \in V_{\text{bot}}} \sum_{v_i:(v_i,v_j)\in E} \mathbf{q}_{ij}(t), \tag{3.5}$$

and $h_{\text{final}} := h(t_{\text{final}})$. The dimensionless accumulated foulant concentration is written as

$$c_{\text{acm}}(t) = \frac{\int_0^t c_{\text{out}}(t')\, q_{\text{out}}(t')\,dt'}{\int_0^t q_{\text{out}}(t')\,dt'}, \tag{3.6}$$

where

$$c_{\text{out}}(t) = \frac{\sum_{v_j \in V_{\text{bot}}} \sum_{v_i:(v_i,v_j)\in E} \boldsymbol{c}_j(t)\,\mathbf{q}_{ij}(t)}{q_{\text{out}}(t)}.$$

4. Algorithm. We summarize the network generation protocol and solution technique for the proposed model equations in Algorithm 4.1. We refer the reader to a worked example in Appendix C for a better visualization of how the governing equations evolve on a very simple network and how our chosen performance metrics depend on the model parameters.

Algorithm 4.1. Filtration with adsorption.

1. Initialization
   (a) Generate uniformly N_{total} random points in box $[0,1]^2 \times [-0.5, 1.5]$.
   (b) Connect all points separated by a distance smaller than d but larger than $d_{\min}$ using the metric χ (periodic or isolated). Discard isolated points.
   (c) Truncate the box with cutting planes at $x_3 = 0$ and $x_3 = 1$; record points with $0 < x_3 < 1$ as the set of interior points V_{int}; label intersections between cutting planes and edges as inlets V_{int} for intersections at $x_3 = 0$ and outlets V_{out} for those at $x_3 = 1$. Set $V = V_{\text{int}} \cup V_{\text{top}} \cup V_{\text{bot}}$.
   (d) Initialize radii $r_{ij,0}$ for $(r_{ij})_{(v_i,v_j)\in E}$.
2. Fluid flow
   (a) Find pressures $\boldsymbol{p}$ and fluxes $\mathbf{q}$ by solving (3.2a)–(3.2c).
3. Foulant concentration
   (a) Initialize concentrations $\boldsymbol{c}_0$ (per (3.3b)) for $v_i \in V_{\text{top}}$.
   (b) Find foulant concentration $\boldsymbol{c}$ by solving (3.3a)–(3.3b).
4. Adsorption
   (a) Evolve each pore radius r_{ij} via (3.4) until it decreases to 0 and stays at 0 for the rest of the filtration.
5. Check *stopping criterion*. Stop if satisfied.
6. Compute throughput using (3.5).
7. Update conductance $\mathbf{k}$ and weighted graph Laplacian $\mathbf{L}_{\mathbf{k}}$.
8. Increment time $t \to t + dt$ and return to (2).

5. Results. In this section, we present numerical results on how filter performance metrics, such as total throughput and accumulative foulant concentration (introduced in subsection 2.7), depend on filter geometry, characterized by three main geometric network parameters detailed below. For each metric/parameter pair considered we first describe the observed trends and compare the results between the isolated and periodic network configurations. Then, we discuss how the findings are related, with a focus on identifying universal parameters that describe filter performance.

5.1. Geometric network parameters. To investigate different network architectures, we introduce three geometric parameters. The first is the average number of neighbors for interior vertices/junctions,

$$N := \frac{|E|}{|V_{\text{int}}|}.$$

This parameter provides one way to characterize the connectivity strength of a network. We compute N only over interior vertices, as any inlet or outlet has exactly one neighbor due to our network generation protocol. Second, the initial void volume,

$$\text{Vol}_0 = \frac{\pi}{2} \sum_{(v_i,v_j)\in E} a_{ij} r_{ij}^2 \,(t=0) = \frac{\pi r_0^2}{2} \sum_{(v_i,v_j)\in E} a_{ij}, \tag{5.1}$$

provides an estimate of how much fluid the filter can process initially, and how much surface area is available for foulant adsorption (since the initial pore radius is the same for all pores, the initial total pore surface area is given by $2\text{Vol}_0/r_0$). Since the representative membrane volume we consider is a unit cube in our dimensionless framework, Vol_0 is exactly the initial membrane *porosity.* Last, we consider tortuosity τ, defined by the *average length of paths* (defined with respect to flow paths) that connect the top and bottom membrane surface through the network, normalized by the membrane thickness (the shortest possible path). A rigorous definition of τ is given in the appendix (Definition B.2 and (B.4)).

Our input parameters (d, N_{total}) (see Algorithm 4.1) are chosen so that the volume and area constraints (initial total pore volume should not exceed that of the representative unit membrane cube, and total pore cross-sectional area on membrane top and bottom surfaces should not exceed the area of the unit square; see section 2.2) are not violated, and so that the generated graphs are nontrivially connected from top to bottom surfaces. The ranges of d and N_{total} are $[0.1, 0.45]$ and $[100, 5000]$, respectively. In all simulations we fix $r_0 = 0.01$, $d_{\min} = 0.06$, $\lambda = 5 \times 10^{-7}$ and produce data curves for each chosen d-value (represented by the same marker) by varying N_{total}.

Due to the random nature of our network generation, we compute the average of quantities of interest over a number of realizations. For simplicity, we do not use additional notation to indicate such averaged quantities. For all results below, each data point is obtained by averaging over 500 simulations, i.e., 500 realizations of a random graph with parameter pair (d, N_{total}). We histogram these 500 realizations in the supplement for each pair (d, N_{total}), to demonstrate that their variance is influenced only by geometric parameters, justifying the sufficiency of this number of realizations. All results are shown for the two cases in which the underlying random graphs are generated with isolated and periodic boundary conditions, with results (data points in blue and red, respectively) compared side-by-side.

5.2. Initial void volume and average number of neighbors. In this section, we present results showing the dependence of performance metrics on two geometric parameters: initial void volume Vol_0 and average number of neighbors N.

Figure 3 shows total throughput h_{final} against initial void volume Vol_0 on a loglog scale, for various d-values. Both quantities are increasing functions of the initially specified number of random points, N_{total}, for each d. In both isolated and periodic cases we see a power law relationship emerge for sufficiently large Vol_0, with good collapse of the data for $\text{Vol}_0 \gtrsim 0.2$, $d \gtrsim 0.2$ onto a single line, hinting at a universal

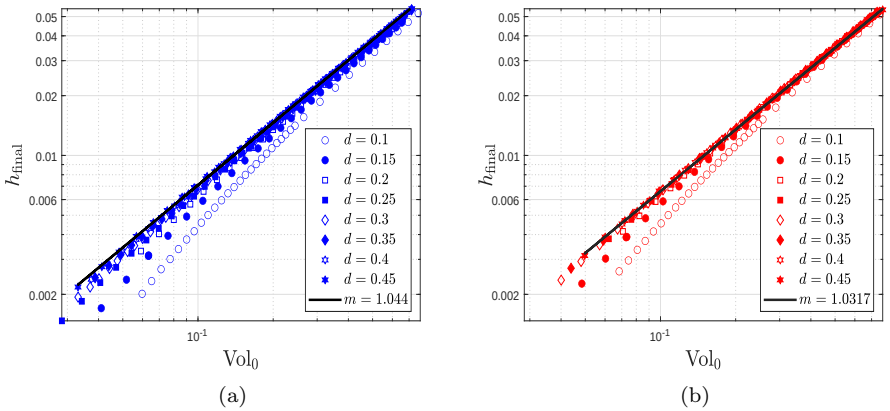

FIG. 3. *Total throughput* h_{final} *versus initial void volume* Vol_0 *(loglog scales).* (a) *Isolated network setup;* (b) *periodic setup. Line of best fit for* $d = 0.45$ *is in black, with gradient* m *given in legend (with* $R^2 = 0.99989$ *and* 0.99993*, respectively). Distribution of error for each data point is given in the histograms in the supplement* (M142474SupMat.pdf [local/web 497KB]).

law. The fact that h_{final} is an increasing function of Vol_0 makes sense because the larger the initial pore volume, the more filtrate can be processed. In both setups, the data curves for smaller d-values begin to deviate from the universal power law for $\text{Vol}_0 \lesssim 0.3$, which enables us to observe some hierarchy. For similar Vol_0-values, corresponding to similar total length of edges per (5.1), we see that larger d-values lead to larger total throughput h_{final}. We attribute this to the fact that networks with larger d-values induce more inlets on the upstream (and downstream) membrane surfaces, allowing more filtrate to pass through. The differences between the isolated and periodic setups in Figure 3 are minor.

In Figures 4(a) and 4(b), we plot total throughput h_{final} against average number of neighbors N (the average number of pores entering or leaving each vertex) for various values of the search radius d, using a log scale for both axes. Each data point shown corresponds to a different choice of N_{total} and, as discussed above, represents results averaged over 500 individual random graph realizations. Several features are common to both plots: first, h_{final} is an increasing function of N for each d-value and, in particular, obeys a power law for sufficiently large N. For fixed N, the smaller the search radius d, the larger the average throughput h_{final}. This suggests that the number of pore junctions plays an important role in controlling and predicting total throughput. Second, the slopes for each d-value at large N are very similar for both isolated and periodic setups, suggesting a common power law relating h_{final} and N for each d (see $d = 0.45$ in Figure 4(a), (b) with slope ≈ 2 in both cases). Moreover, as d increases the curves in Figure 4(a), (b) become more closely spaced in both setups, demonstrating that filters with sufficiently large search radius perform similarly in terms of total throughput. In both cases the quantities N and h_{final} are increasing functions of N_{total} for each d.

We also highlight the differences between the two compared network connection metrics in Figures 4(a) and 4(b). First, for small d (e.g., $d = 0.1, 0.15$), the isolated and periodic networks give similar throughputs since random graph generations under the two metrics do not differ greatly; however, as d increases, the periodic metric generates more edges than the isolated one (for the same value of N_{total}), hence the periodic setup yields higher throughput. By the same reasoning, for fixed h_{final}, N

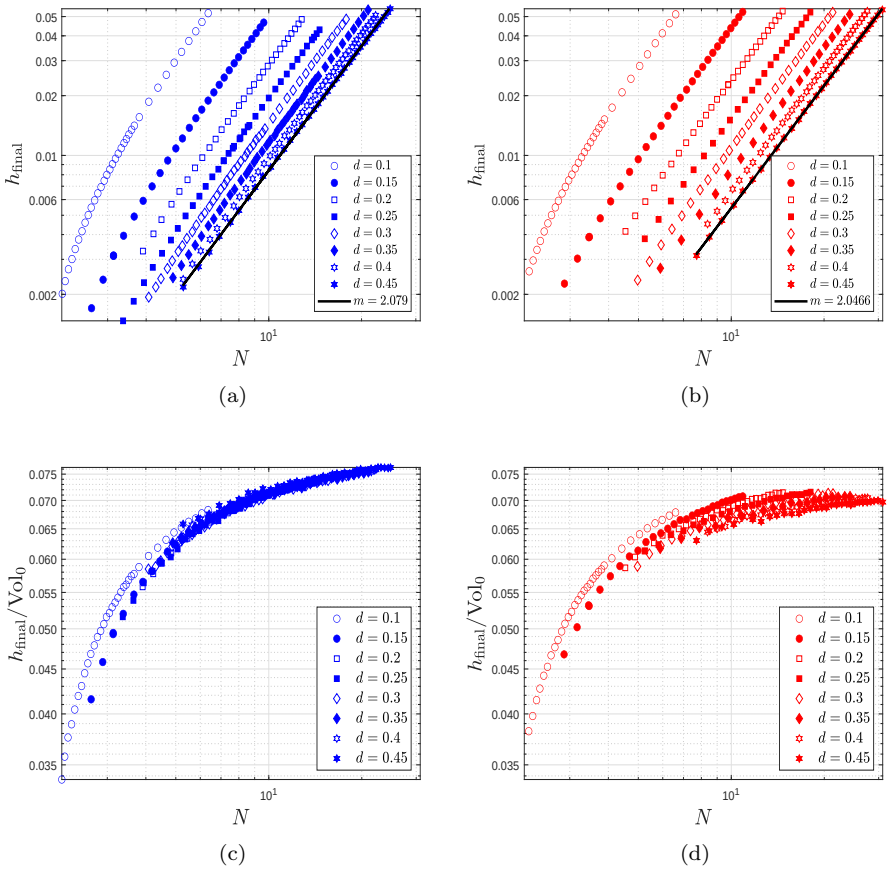

FIG. 4. *Total throughput* h_{final} *versus average number of neighbors* N *(loglog scales).* (a) *Isolated network setup;* (b) *periodic setup. Line of best fit for* $d = 0.45$ *is in black, with gradient* m *given in legend. Distribution of error for each data point is given in the histograms in the supplement* (M142474SupMat.pdf [local/web 497KB]). *Same setup for* (c) *and* (d) *with* $h_{\text{final}}/\text{Vol}_0$ *as vertical axis (loglog scales).*

is much larger in the periodic setup than in the isolated one for each $d \gtrsim 0.3$ (the data curves in the isolated setup are seen to be more closely spaced than those in the periodic setup as d increases). In other words, though N is an increasing function of d in each setup, it increases at a higher rate under the periodic metric.

Motivated by the strong relationship between total throughput and volume found in Figure 3, we also plot volume-scaled total throughput, $h_{\text{final}}/\text{Vol}_0$, against average number of neighbors N for both connection metrics in Figures 4(c) and 4(d). This volume-scaled total throughput can be understood as a measure of efficiency of the membrane filter in terms of filtrate production capability. In Figure 4(c), we observe a good collapse of data in the nonperiodic setup, which suggests that the average number of neighbors is a good predictor for total throughput scaled by volume. We see a similar trend in Figure 4(d) for the periodic setup, though the collapse is less strong. We further note that in both nonperiodic and periodic setups, data for $d = 0.1$ are slightly separated from the rest. This is consistent with the deviation of data for $d = 0.1$ in Figure 3 from the universal power law relating total throughput and volume.

Figure 5 shows final accumulated foulant concentration in the filtrate, $c_{\text{acm}}(t_{\text{final}})$, versus initial void volume, Vol_0, on a loglog scale, as d is varied. Both quantities are

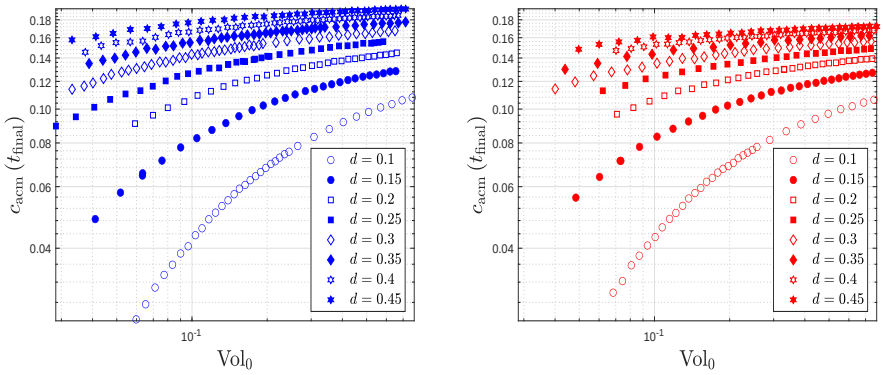

FIG. 5. *Final accumulated foulant concentration* $c_{\mathrm{acm}}(t_{\mathrm{final}})$ *versus initial void volume* Vol_0 *(loglog scales).* (a) *Isolated network setup;* (b) *periodic setup. Distribution of error for each data point is given in the histograms in the supplement* (M142474SupMat.pdf [local/web 497KB]).

increasing functions of N_{total} for each d. The plots for both isolated and periodic network metrics show that $c_{\mathrm{acm}}(t_{\mathrm{final}})$ increases as search radius d increases for fixed Vol_0. This is because with similar initial pore volume and thus similar initial total edge length, networks with larger d have fewer edges to which foulants can adhere. Combining this finding with the result in Figure 3 for a fixed volume further confirms the intuition that networks producing larger throughput (larger d) also have worse foulant control. A second trait shared by both network setups is that for larger d (for example, $d = 0.4, 0.45$), $c_{\mathrm{acm}}(t_{\mathrm{final}})$ is relatively insensitive to changes in Vol_0, while for smaller d (say, $d = 0.1, 0.15$), the change in $c_{\mathrm{acm}}(t_{\mathrm{final}})$ with Vol_0 is much more dramatic. This says that in membrane networks with longer pores, final accumulated foulant concentration depends less on initial void volume than in networks with shorter pores. We further observe that for a given Vol_0, for small d, the values of $c_{\mathrm{acm}}(t_{\mathrm{final}})$ are similar for both isolated and periodic configurations. However, as d increases, the isolated case incurs larger $c_{\mathrm{acm}}(t_{\mathrm{final}})$ and thereby exhibits worse foulant control than the periodic case. We defer further discussion of this observation to subsection 5.3. Last, we find that in practice, when a tolerance level of contaminant concentration in the filtrate is specified in Figure 5, networks with smaller d-values have larger initial pore volume, which corresponds to larger total throughput via the strong relationship observed in Figure 3 (e.g., if a threshold of $c_{\mathrm{acm}}(t_{\mathrm{final}}) = 0.06$ is set, filters with $d = 0.1$ are preferable as they have larger initial pore volume and thus larger total throughput).

5.3. Tortuosity. We now examine the dependence of our performance metrics on initial network tortuosity τ, the average distance traveled by a fluid particle from the top membrane surface to the bottom, before any fouling has occurred. A full characterization of τ is given by Definition B.2 and (B.4) in the appendix.

Our main result is that tortuosity is an important universal parameter that predicts accumulated foulant concentration independently of input parameters (d, N_{total}). Figures 6(a) and 6(b) plot accumulated foulant concentration in the filtrate, $c_{\mathrm{acm}}(t_{\mathrm{final}})$, versus tortuosity, τ, for various values of the search radius d. We readily observe the similar collapse of data points in both cases, particularly strongly in the isolated case. We find that $c_{\mathrm{acm}}(t_{\mathrm{final}})$ decays exponentially with τ, with a negative exponent, which implies that networks with more winding flow paths make much

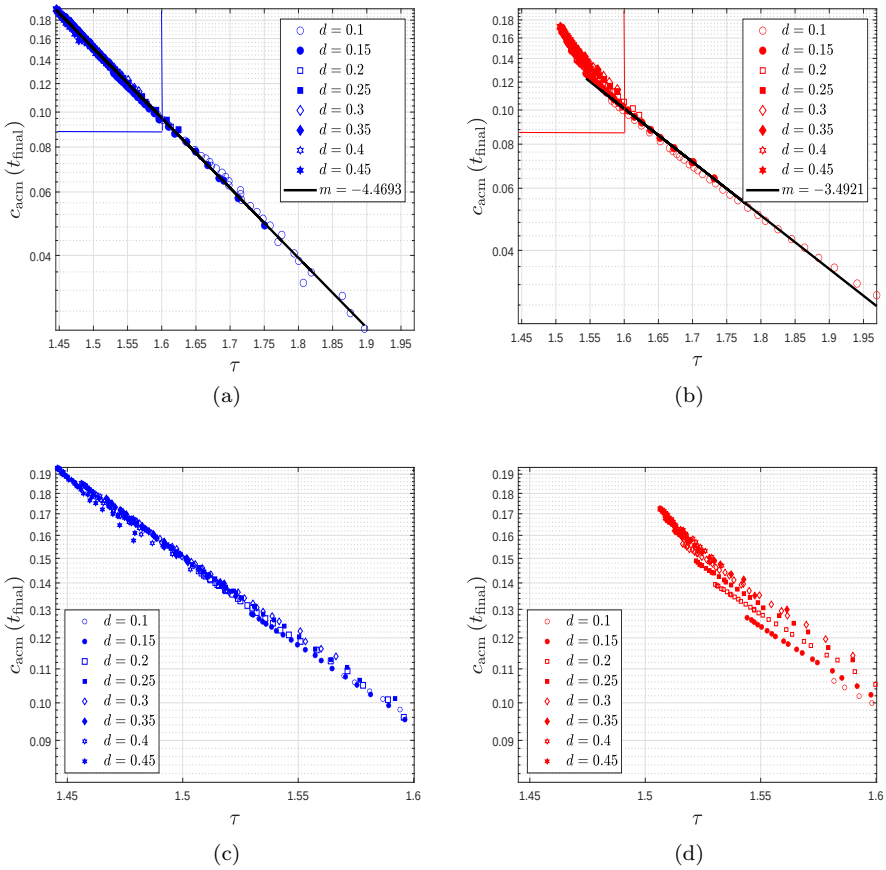

FIG. 6. *Final accumulated foulant concentration* $c_{\mathrm{acm}}(t_{\mathrm{final}})$ *versus tortuosity* τ *(semilog plot).* (a) *Isolated network setup;* (b) *periodic setup. The line of best fit is in black in each plot, with gradient* m *given in the legend (with* $R^2 = 0.99838$ *and* 0.9961*, respectively). The blue and red boxes at top left are shown as zooms in* (c) *and* (d)*, respectively, for small tortuosity values (same data as* (a) *and* (b)*, respectively). Distribution of error for each data point is given in the histograms in the supplement* (M142474SupMat.pdf [local/web 497KB]).

better filters in terms of foulant control. This is because the extent of deposition (per (2.18)) increases as distance traveled by the fluid increases. We also observe two further details: within the regime where the fit (solid black line) is strongest in the plots, the data for the isolated setup (Figure 6(a)) has a larger (negative) slope than that in the periodic setup (Figure 6(b)); and, for fixed τ, filters in the periodic setup have slightly higher accumulated foulant concentration.

Figures 6(c) and 6(d) show zoomed plots of the data from Figures 6(a) and 6(b), respectively, to probe the details of the low tortuosity regime, where accumulated foulant concentration is highest. To facilitate the discussion below, note that for each d, a larger value of N_{total} corresponds to a smaller tortuosity τ (i.e., adding more vertices to the network decreases average path length). Figure 6(d) shows that for the periodic pore network we see an emergent nonlinear trend, breaking the exponential relation between $c_{\mathrm{acm}}(t_{\mathrm{final}})$ and τ as N_{total} is increased. Although the isolated setup in Figure 6(c) appears to persist in its linear (exponential relationship) trend, we note

that for yet larger values of N_{total} this trend must break down due to the existence of a lower bound, $\tau_{\min}$, on tortuosity. While there is a trivial lower bound, $\tau_{\min} \geq 1$ for each setup, in Appendix B we show that bounds can be tightened to approximately 1.128 for the isolated setup and 1.304 for the periodic one. The bound is larger for the periodic case because, for a fixed set of vertices, the additional paths obtained from the periodic setup are on average longer, as they can penetrate through the boundaries; see Appendix B. Our simulations cannot access the breakdown in the power law for the isolated case because, for the large values of N_{total} required to access this regime, we increasingly often violate the volume constraint for individual realizations of the random network.

Figure 7 shows total throughput h_{final} versus tortuosity τ for various d-values, on a semilog scale. We note that h_{final} decreases as τ increases for each d because if the feed solution traverses longer paths (on average) through the filter, then it deposits more foulant and thus pores close faster. Second, for fixed h_{final}, larger d corresponds to smaller τ. Combining this finding with the results in Figure 6, we reach the following conclusion: between two membrane networks that produce the same total throughput, the one with shorter characteristic pore length (smaller d) is favored since it also has larger tortuosity and thus better foulant control. Last, in both Figures 7(a) and 7(b), we see again the clear evidence of a limiting tortuosity $\tau_{\min} > 1$: in the data curves for each $d \geq 0.35$, τ does not vary greatly as we vary N_{total}.

Now, we highlight the differences in Figure 7: first, for a fixed tortuosity τ (at a given d-value), h_{final} in the isolated setup (Figure 7(a)) is lower than in the periodic one (Figure 7(b)), because the periodic boundary conditions give rise to more edges and hence a larger initial void volume Vol_0. We confirm this reasoning by plotting Vol_0 against τ in Figure 8. There, when we fix τ for each value of d, we observe a higher initial volume for the periodic case than the isolated one. This observation also explains why accumulated foulant concentration is higher in the periodic case for a fixed τ (per Figure 6) because networks with periodic boundary conditions, by having larger initial volume, process more filtrate (larger throughput), which leads to a greater quantity of foulant escaping the filter. This reasoning also explains the difference between $c_{\text{acm}}(t_{\text{final}})$ in Figures 5(a) and 5(b) by fixing Vol_0 for each d.

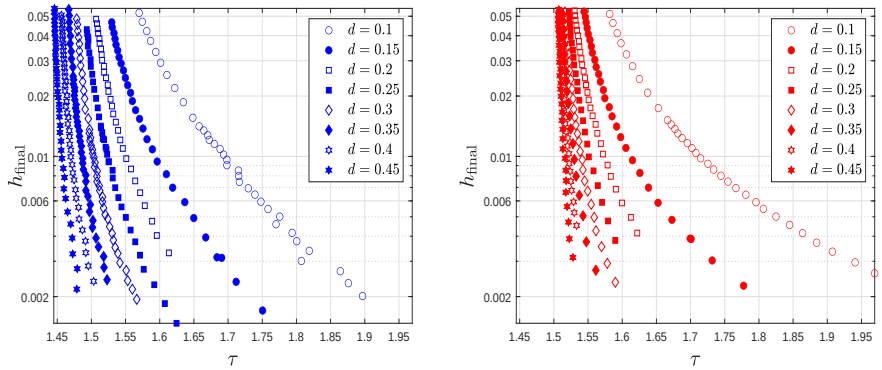

(a) (b)

FIG. 7. *Total throughput h_{final} versus tortuosity τ (semilog plot).* (a) *Isolated setup;* (b) *periodic setup. Error distribution for each data point is provided in the supplement* (M142474SupMat.pdf [local/web 497KB]). *Same scale for h_{final} as in Figure* 3.

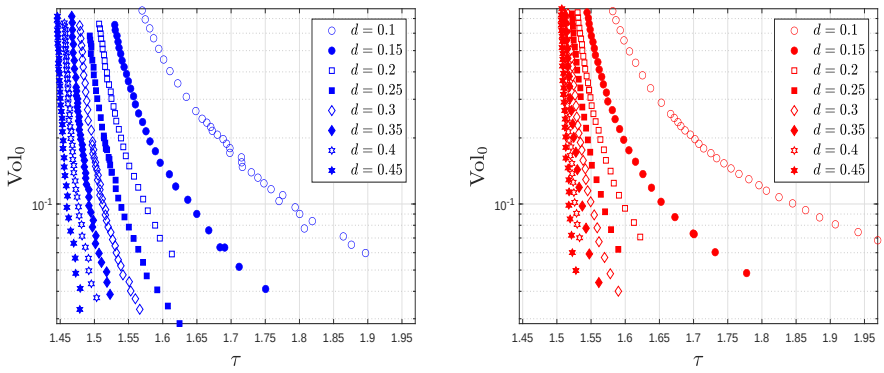

FIG. 8. *Initial void volume versus tortuosity (semilog plot).* (a) *Isolated setup;* (b) *periodic setup. Error distribution for each data point is provided in the supplement* (M142474SupMat.pdf [local/web 497KB]).

6. Conclusions. We here summarize our findings on the connections between performance metrics of the network/filter and each characteristic geometric network parameter, and highlight areas for future work. We first collect our main findings:

1. Initial void volume Vol_0 is a good predictor of total throughput h_{final}, particularly when $\mathrm{Vol}_0 > 0.5$, when there appears to be a power law relation between the two quantities (per Figure 3). Average number of neighbors N is also correlated with h_{final} but is a weaker predictor in this respect than Vol_0 (per Figure 4).
2. Tortuosity τ fully characterizes final accumulated foulant concentration c_{acm} (t_{final}) in the filtrate by a negative exponential relationship. See Figure 6.
3. When a minimum concentration requirement is imposed, membrane filters with small characteristic pore length should be considered since they have larger void volume and thus process more filtrate. See Figure 5.
4. When two membrane networks produce the same final throughput h_{final}, the one with shorter characteristic pore length should be favored, since it will have higher tortuosity and thus better foulant control. See Figure 8.

Griffiths et al. [10] showed that the particle removal efficiency, corresponding equivalently to $1 - c_{\mathrm{acm}}\,(t_{\mathrm{final}})$ in our setup, increases as tortuosity increases, a trend consistent with our conclusion here regarding the negative exponential relationship between accumulated foulant concentration and tortuosity, though the exact relationship in both approaches is different (negative subexponential in that work [10]). Such differences may originate from the different graph generation protocols used in the two works.

We also find that the choice of network connection metric (isolated versus periodic) may significantly affect how the network functions as a filter. With identical input parameters N_{total} (representing the number of initial random points generated) and d (the search radius, or maximum edge length), the periodic setup yields larger average number of neighbors and thus higher connectivity. This is important, since the periodic setup provides a more realistic representation of a (large) membrane.

In recent years, many modern imaging techniques to study material properties have been developed which, in turn, provide fertile ground for graphical modeling approaches to membrane filtration and analysis of membrane performance. For example,

Jimenez-Martinez and Negre [14] have outlined a topological algorithm (Figure 1 in their paper) that translates a 2D image of a membrane cross section into a pore network. The idea is to take an original binary image where black and white represent membrane void and materials (resp.), and then construct a distance-to-nearest-object function (the DNO function) that computes the distance between a pixel to its nearest object (membrane material). Then, the location of pore junctions is determined by the local maxima of the DNO function, while the width of the edges connecting the junctions is determined by the minimal distance normal to the edge. For other techniques, see Sun et al. [20] and Sundaramoorthi et al. [21].

In future work, as well as utilizing some of the image analysis methods outlined above to generate more realistic networks, we plan to consider network models of membrane filters that include pore size variations, providing a more accurate representation of real membrane filters, due to inevitable manufacturing defects/inhomogeneities. We plan also to incorporate other fouling modes, such as blocking or sieving by large particles that may occlude pores, unaccounted for in this work. Including such large-particle blocking will add new dimensions of stochastic complexity to our modeling. In particular, a model that includes both extensions listed above may exhibit internal blockage at an earlier stage than the closure of top inlets (as always observed in our work here) when pore size variations are sufficiently large, leading to much more complex flow and fouling behavior. Our graphical description of the problem will allow us to investigate problems of this type in a systematic and computationally efficient manner.

Appendix A. Justification for pore radius evolution model. In this section, we justify the form of the pore radius evolution equation (2.26) using the (exact) solution for the foulant concentration model, (2.18), to relate the rate of change of particle volume accretion inside a single pore to pore radius shrinkage. In the following derivation, we drop the indices ij for notational simplicity and assume that the radius R is spatially constant at each time T (though the arguments can be adapted to the variable radius case with a suitable bound on $\partial R/\partial Y$).

Let V_p be the particle volume. In a single pore (assumed circularly cylindrical), we consider an infinitesimally thin circular disk at distance Y from the pore inlet, with thickness dY. The particle flux difference across this disk is

$$(C(Y+dY,T)-C(Y,T))\,\mathbf{Q}(T)\approx\frac{\partial C}{\partial Y}(Y,T)\,\mathbf{Q}(T)\,dY, \tag{A.1}$$

i.e., the number of particles per time deposited in the disk. The total particle volume adsorped in this pore is V_p times this quantity. We integrate (A.1) over the length of the pore to obtain the total volume of deposited particles per time in the pore,

$$V_p\mathbf{Q}(T)\int_0^A\frac{\partial C}{\partial Y}(Y,T)\,dY=V_p\mathbf{Q}(T)\left[C(A,T)-C(0,T)\right] \tag{A.2a}$$

$$=V_p\mathbf{Q}(T)\,\boldsymbol{C}(T)\left(\exp\left(-\frac{\Lambda R(T)\,A}{\mathbf{Q}(T)}\right)-1\right) \tag{A.2b}$$

$$\approx -V_p\boldsymbol{C}(T)\,\Lambda R(T)\,A, \tag{A.2c}$$

where we used the analytical expression (2.18) for $C(Y,T)$ in the second equality. The final approximate Taylor expansion (A.2c) is justified for sufficiently small values of the exponent, that is (using the scales in section 3), provided

$$\mathbf{q}(t)\gg\lambda r_0 d, \tag{A.3}$$

where d is the largest pore length (see (2.1)).

As foulant particle volume accumulates at the rate given in (A.2c), pore volume $\mathrm{Vol}\,(T)$ also changes at this rate via

$$\frac{d\mathrm{Vol}\,(T)}{dT} = -V_p \boldsymbol{C}\,(T)\,\Lambda R\,(T)\,A. \tag{A.4}$$

At the same time, we relate the volume of the pore to its radius $\mathrm{Vol}\,(T) = \pi R^2\,(T)\,A$ and obtain

$$\frac{d\mathrm{Vol}\,(T)}{dT} = 2\pi R\,(T)\,\frac{dR}{dT} A. \tag{A.5}$$

Equating (A.4) and (A.5), we arrive at the form of (2.26) with $\alpha = \frac{V_p}{2\pi}$.

Appendix B. Tortuosity. In this section, we define tortuosity of a graph representing a membrane filter pore network and provide an explicit formula using the geometric and initial flow information from the network (found in section 2). In all of our investigations we restrict attention to the tortuosity of the initial pore network, with no regard for how it subsequently evolves under fouling, hence in the following discussion it should be understood that we consider properties of the network at time $t = 0$.

We define tortuosity as the average distance travelled by a fluid particle through the membrane via the network, relative to the thickness of membrane W. Now, given a path from any inlet to any outlet, we can associate it with its total initial flux, which we use as a weight for the path. This is equivalent to having the fluid particle perform a discrete random walk on the graph G directed by fluid flux at each junction. More precisely, the transition matrix $\mathbf{P}$ of this random walk is defined as follows. We omit the argument of $t = 0$ for notational simplicity.

We first enforce nonnegativity of the flux matrix via the following modification. Consider $\mathbf{Q}_+$ and $\mathbf{Q}_-$, the positive and negative parts of $\mathbf{Q}$, respectively, such that $\mathbf{Q} = \mathbf{Q}_+ + \mathbf{Q}_-$. Owing to the skew-symmetry of $\mathbf{Q}$, we construct

$$\tilde{\mathbf{Q}} = \mathbf{Q}_+ - \mathbf{Q}_-^T, \tag{B.1}$$

which preserves the flow information (direction and magnitude) while enforcing nonnegativity.

Definition B.1 (transition matrix). *Given modified flux matrix* $\tilde{\mathbf{Q}}$ *in* (B.1)*, the transition matrix* $\mathbf{P}$ *is determined by rescaling* $\tilde{\mathbf{Q}}$ *by its row sum:*

$$\mathbf{P}_{ij} = \begin{cases} \dfrac{\tilde{\mathbf{Q}}_{ij}}{\displaystyle\sum_{v_j:(v_i,v_j)\in E} \tilde{\mathbf{Q}}_{ij}}, & (v_i, v_j) \in E, \quad v_i \in V_{\mathrm{top}} \cup V_{\mathrm{int}}, \\ 1, & v_i \in V_{\mathrm{bot}}, \quad j = i, \\ 0 & \textit{otherwise.} \end{cases} \tag{B.2}$$

For vertices in the bottom surface, fluid particles are absorbed, i.e., once they reach any $v \in V_{\mathrm{bot}}$*, they stay there with probability one.*

Let X_n be a random walk with transition $\mathbf{P}$, i.e., X_n is the vertex after the fluid particle has taken n steps on V. Let $\mathbb{P}$ be the induced probability measure. This random walk has a natural initial distribution (a column vector of length $|V|$),

$$\pi_{0i} = \mathbb{P}\{X_0 = v_i\} := \begin{cases} \dfrac{\displaystyle\sum_{v_j:(v_i,v_j)\in E} \tilde{\mathbf{Q}}_{ij}}{\displaystyle\sum_{v_i\in V_{\text{top}}} \sum_{v_j:(v_i,v_j)\in E} \tilde{\mathbf{Q}}_{ij}}, & v_i \in V_{\text{top}}, \\ 0 & \text{otherwise}, \end{cases} \tag{B.3}$$

namely, the probability of going to each inlet on the top surface is determined by the proportion of flux going through that inlet, relative to total flux.

DEFINITION B.2 (tortuosity). *Let l_n be the total path length after the random walk has taken n steps. Tortuosity of the graph G is defined by $\mathbb{E}[\tau]$ where $\tau := \frac{l_m}{W}$ and m is the (deterministic) number of steps of the longest path from any inlet on the top surface to any outlet in the bottom surface.*

The integer m can be understood as a graph diameter where the notion of graph distance for m is encoded in the unweighted adjacency matrix $\mathbf{W}$ (entries are indicators of the existence of an edge). m is trivially bounded above by $|V_{\text{int}}| + 2$ (one step from V_{top} to V_{int} and V_{int} to V_{bot}, respectively, and traverse all of V_{int} at worst), which we use here. Although this bound can be tightened by connectivity measures such as the smallest number of vertices that must be removed to disconnect a graph (see Coll et al. [5], for example), our algorithm (discussed after proving the formula (B.4)) for $\mathbb{E}[\tau]$ does not incur significant computational cost from the size of m.

One may estimate this expected value by sending a large number of particles through the network and computing the average of path lengths. We here provide an explicit formula for $\mathbb{E}[\tau]$ that depends on the transition matrix $\mathbf{P}$ and a distance weight matrix $\mathbf{W}_E$, whose entries are

$$\mathbf{W}_{E,ij} = \begin{cases} \chi(v_i, v_j), & (v_i, v_j) \in E, \\ 0 & \text{otherwise}, \end{cases}$$

where $\chi(v_i, v_j)$ is the distance between vertices v_i and v_j via the metric χ defined in (2.2). Using this formula directly obviates the use of large-number-of-particle simulations and thus reduces computational load significantly.

PROPOSITION B.3 (tortuosity formula).

$$\mathbb{E}[\tau] = \frac{1}{W}\mathbb{E}[l_m] = \frac{\pi_0^{\mathrm{T}}}{W}\left(\sum_{n=1}^{m} \mathbf{P}^{n-1}\right) \operatorname{diag}(\mathbf{P}\mathbf{W}_E), \tag{B.4}$$

where $\operatorname{diag}(A)$ *is a column vector that lists the diagonal elements of a matrix A.*

Proof. We compute $\mathbb{E}[l_m]$. Denote the conditional probability and expectation

$$\mathbb{P}[\cdot \mid X_0 = i] = \mathbb{P}_i[\cdot], \quad \mathbb{E}[\cdot \mid X_0 = i] = \mathbb{E}_i[\cdot].$$

First, we observe by the law of total expectation that

$$\mathbb{E}[l_m] = \sum_{i=1}^{|V|} \mathbb{E}[l_m \mid X_0 = i]\,\mathbb{P}\{X_0 = i\} = \sum_{i=1}^{|V|} \mathbb{E}_i[l_m]\,\pi_{0i} := \pi_0^{\mathrm{T}}\boldsymbol{U},$$

where π_0 is given by (B.3) and $\boldsymbol{U} := (\mathbb{E}_i[l_m])_{v_i\in V}$. We now focus on an arbitrary element of $\boldsymbol{U}$. Noting that $\mathbb{E}_i[L_0] = 0$, and using linearity of expectation, the law of

total expectation, the Markov property of the random walk and symmetry of $\mathbf{W}_E$, we have

$$\begin{aligned}\mathbb{E}_i[l_m] &= \mathbb{E}_i\left[\sum_{n=1}^{m}(l_n - l_{n-1})\right] = \sum_{n=1}^{m}\mathbb{E}_i(l_n - l_{n-1}) \\ &= \sum_{n=1}^{m}\sum_{j\in V}\mathbb{E}_i(l_n - l_{n-1} \mid X_{n-1} = j)\,\mathbb{P}_i(X_{n-1} = j) \\ &= \sum_{n=1}^{m}\sum_{j\in V}\left(\sum_{k\in V}\mathbf{W}_{E,jk}\mathbf{P}_{jk}\right)\mathbf{P}_{ij}^{(n-1)} = \sum_{n=1}^{m}\sum_{j\in V}\mathbf{P}_{ij}^{(n-1)}\left(\mathbf{P}\mathbf{W}_E\right)_{jj},\end{aligned}$$

where $\mathbf{P}_{ij}^{(k)}$ is the kth iterate of $\mathbf{P}$. Thus, in matrix form,

$$\boldsymbol{U} = \sum_{n=1}^{m}\sum_{j\in V}\begin{pmatrix}\mathbf{P}_{1j}^{(n-1)}\\ \cdot\\ \cdot\\ \cdot\\ \mathbf{P}_{|V|j}^{(n-1)}\end{pmatrix}\left(\mathbf{P}\mathbf{W}_E\right)_{jj} = \left(\sum_{n=1}^{m}\mathbf{P}^{n-1}\right)\operatorname{diag}\left(\mathbf{P}\mathbf{W}_E\right),$$

using the fact that $\mathbf{P}^{(n-1)} = \mathbf{P}^{n-1}$, completing the proof. ∎

In practice, to avoid taking large matrix powers when evaluating (B.4), we have devised a fast algorithm in evaluating the geometric series $\sum_{n=1}^{m}\mathbf{P}^{n-1}$, by appealing to a geometric sum formula on matrices involving matrix inversions. We utilize the block upper triangular structure of $\mathbf{P}$ by block partitioning into components (known as a *divide and conquer*–type scheme) including the identity block in its southeast corner, to ease the computational load of inversions. Naive evaluation of the series is of complexity $O(m|V|^3)$ (cubic term from matrix multiplication and m additions), while our algorithm is $O(|V|^3)$.

We argue that the constant initial radius assumption on the pores deems τ a geometric parameter independent of fluid flow, even though its definition requires initial flow information and geometric information such as a distance weighted adjacency (see (B.4)). In essence, we claim that τ does not vary too much until the filtration stopping criterion. First, foulant concentration is monotonically decreasing along each edge, and thus the radii of all inlets, under the influence of foulant concentration in the feed solution (see (3.3b)), go to zero earlier than all other downstream channels. Thus, adjacencies of the network do not change until the filter top surface is clogged. Second, though outflowing flux from an arbitrary junction changes over time as the filter fouls, the relative contribution from each outgoing edge does not vary greatly. Altogether, we believe that tortuosity does not depend heavily on the time of filtration but only on the initial geometry of the network. This feature makes tortuosity a universal parameter for foulant concentration.

Last, we note that a theoretical limit exists for tortuosity for both setups. As $N_{\text{total}} \to \infty$ (so that the membrane interior and top and bottom surfaces are uniformly densely packed with pore junctions), we can provide a simple lower bound for the limit in the following sense. Consider an arbitrary inlet-outlet pair. They will be connected by a path with vertical component 1. For the isolated setup, the horizontal component can be estimated as the average distance between two uniformly random points in two dimensions in a unit square and is about 0.521 (length of YK in Figure 9(a)).

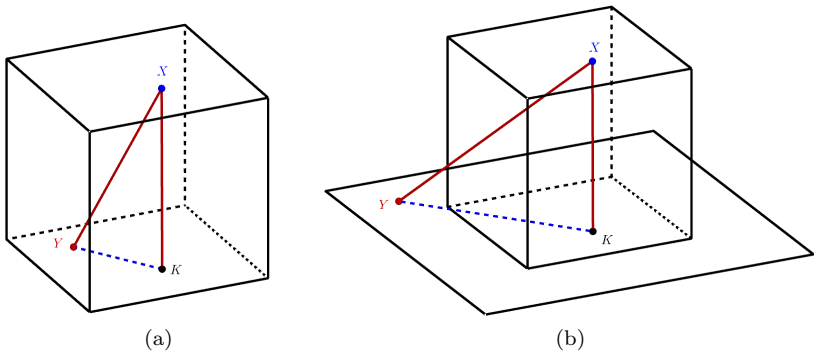

FIG. 9. *Tortuosity limit:* (a) *Isolated setup (unit cube);* (b) *periodic setup (unit cube and a square of side length* 2 *containing the bottom surface of the unit cube). X (blue) and Y (red) are uniformly sampled from the top and bottom membrane surfaces, respectively. K (black) in both figures is the projection of X onto the bottom surface; XK in both figures has length* 1.

Together, these numbers provide a lower bound for the limiting tortuosity $\tau_{\min}$ of around $1.128 = \sqrt{1^2 + 0.521^2}$ for the isolated case. The argument for the periodic case is slightly more elaborate—while the vertical component of an average path is still 1, the horizontal component now is the average distance between two random points uniformly sampled from the squares $[0.5, 1.5]^2$ and $[0, 2]^2$, respectively (found to be 0.838, the length of YK in Figure 9(b)); thus an average path length is about 1.304. The difference arises because with the periodic metric, any inlet uniformly sampled from a unit square can potentially connect to outlets that are outside the unit square (bottom surface) but within 0.5 distance to the boundary (due to the constraint that search radius $d < 0.5$). These arguments provide some justification for the observations that the tortuosity in the periodic case may be larger than the isolated case. The numerical values given above are obtained by standard probabilistic calculations and numerical integration. We look forward to a more theoretical study of how tortuosity is affected by the initial number of points, the search radius, and the underlying metric.

Appendix C. Worked example. In this section, we provide an example of a simple network (see Figure 10) to illustrate how the governing equations described in subsections 2.3–2.6 depend on the model parameters. The network is a reflected Y-shape, with two inlets and outlets of length $1/2$ and one interior edge of length $1/3$.

Each edge has conductance $\mathbf{k}_{ij}(t)$ per (3.1). For this network, the conductance-weighted graph Laplacian, acting on the pressures at interior vertices, yields the graph Laplace equation (2.15),

$$\text{(C.1)}\quad L_{\mathbf{k}}\boldsymbol{p}(t) = \begin{bmatrix} \mathbf{k}_{13}(t) + \mathbf{k}_{23}(t) + \mathbf{k}_{34}(t) & -\mathbf{k}_{34}(t) \\ -\mathbf{k}_{34}(t) & \mathbf{k}_{34}(t) + \mathbf{k}_{45}(t) + \mathbf{k}_{46}(t) \end{bmatrix} \begin{bmatrix} p_2(t) \\ p_3(t) \end{bmatrix} = \begin{bmatrix} \mathbf{k}_{13}(t) + \mathbf{k}_{23}(t) \\ 0 \end{bmatrix},$$

where the final equality incorporates the boundary conditions (3.2b). Then, the fluxes $\mathbf{q}_{ij}$ satisfy

$$\mathbf{q}_{13}(t) = \mathbf{k}_{13}(t)\left(1 - p_3(t)\right),$$
$$\mathbf{q}_{23}(t) = \mathbf{k}_{23}(t)\left(1 - p_3(t)\right),$$

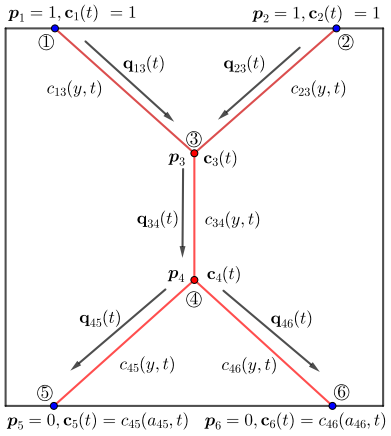

FIG. 10. *2D schematic of a reflected-Y network with labeled physical quantities presented in section 3.*

$$\begin{aligned}
\mathbf{q}_{34}(t) &= \mathbf{k}_{34}(t)\left(p_3(t) - p_4(t)\right), \\
\mathbf{q}_{45}(t) &= \mathbf{k}_{45}(t)\, p_4(t), \\
\mathbf{q}_{46}(t) &= \mathbf{k}_{46}(t)\, p_4(t).
\end{aligned}$$

To proceed, we then solve (3.3a) (the advection graph Laplace equation) to find the foulant concentration at each vertex,

$$\text{(C.2)}\quad L_{\mathbf{q}}^{\text{in}}\boldsymbol{c} = \begin{bmatrix} \mathbf{q}_{13}+\mathbf{q}_{23} & 0 & 0 & 0 \\ -\mathbf{q}_{34}\mathbf{b}_{34} & \mathbf{q}_{34} & 0 & 0 \\ 0 & -\mathbf{q}_{45}\mathbf{b}_{45} & \mathbf{q}_{45} & 0 \\ 0 & -\mathbf{q}_{46}\mathbf{b}_{46} & & \mathbf{q}_{46} \end{bmatrix} \begin{bmatrix} c_3(t) \\ c_4(t) \\ c_5(t) \\ c_6(t) \end{bmatrix}$$
$$= (\mathbf{q}\circ\mathbf{b})^{\mathrm{T}}\boldsymbol{c}_0 = \begin{bmatrix} \mathbf{q}_{13}\mathbf{b}_{13} & \mathbf{q}_{23}\mathbf{b}_{23} \\ 0 & 0 \\ 0 & 0 \\ 0 & 0 \end{bmatrix} \begin{bmatrix} 1 \\ 1 \end{bmatrix} = \begin{bmatrix} \mathbf{q}_{13}\mathbf{b}_{13}+\mathbf{q}_{23}\mathbf{b}_{23} \\ 0 \\ 0 \\ 0 \end{bmatrix},$$

where the third equality uses the boundary condition (3.3b).

After obtaining the concentrations $c_i(t)$ for each vertex, we evolve edge radius via (3.4).

By appealing to the symmetry of this network, one may reduce the system for the dynamics of network evolution to a system of two nonautonomous nonlinear ordinary differential equations, describing the radius evolution $r_{34}(t)$ and $r_{45}(t)$ (which by symmetry is equal to $r_{46}(t)$), with a closed solution for the linear shrinkage rate of $r_{13}(t) = r_{23}(t)$. Since our principal concern here is the end state of the network, we do not present or study this system here.

REFERENCES

[1] P. APEL, *Track etching technique in membrane technology*, Radiat. Meas., 34 (2001), pp. 559–566, https://doi.org/10.1016/S1350-4487(01)00228-1.

[2] A. BONATO, M. LOZIER, D. MITSCHE, X. PÉREZ-GIMÉNEZ, AND P. PRAŁAT, *The domination number of on-line social networks and random geometric graphs*, in Theory and Applications of Models of Computation, Lecture Notes in Comput. Sci. 9076, R. Jain, S. Jain,

and F. Stephan, eds., Springer, New York, 2015, pp. 150–163, https://doi.org/10.1007/978-3-319-17142-5_14.

[3] S.-S. Chang and M. Roper, *Microvascular networks with uniform flow*, J. Theoret. Biol., 462 (2019), pp. 48–64, https://doi.org/10.1016/j.jtbi.2018.10.049.

[4] A. Chapman and M. Mesbahi, *Advection on graphs*, in Proceedings of the 50th IEEE Conference on Decision and Control, 2011, pp. 1461–1466, https://doi.org/10.1109/CDC.2011.6161471.

[5] V. E. Coll, J. Hook, C. Magnant, K. B. McCready, and K. Ryan, *The proper diameter of a graph*, Discuss. Math. Graph Theory, 40 (2020), pp. 107–125, https://doi.org/10.7151/dmgt.2115.

[6] R. M. Colombo, G. Guerra, M. Herty, and V. Schleper, *Optimal control in networks of pipes and canals*, SIAM J. Control Optim, 48 (2009), pp. 2032–2050, https://doi.org/10.1137/080716372.

[7] J. Dall and M. Christensen, *Random geometric graphs*, Phys. Rev. E, 66 (2002), 016121, https://doi.org/10.1103/PhysRevE.66.016121.

[8] T. Eren, *The effects of random geometric graph structure and clustering on localizability of sensor networks*, Int. J. Distrib. Sens. Netw., 13 (2017), https://doi.org/10.1177/1550147717748898.

[9] L. J. Grady, *Discrete Calculus: Applied Analysis on Graphs for Computational Science*, Springer, New York, 2010.

[10] I. M. Griffiths, I. Mitevski, I. Vujkovac, M. R. Illingworth, and P. S. Stewart, *The role of tortuosity in filtration efficiency: A general network model for filtration*, J. Membr. Sci., 598 (2020), 117664, https://doi.org/10.1016/j.memsci.2019.117664.

[11] B. Gu, D. R. Renaud, P. Sanaei, L. Kondic, and L. J. Cummings, *On the influence of pore connectivity on performance of membrane filters*, J. Fluid Mech., 902 (2020), A5, https://doi.org/10.1017/jfm.2020.520.

[12] Y. Hatano, A. K. Das, and M. Mesbahi, *Agreement in presence of noise: pseudogradients on random geometric networks*, in Proceedings of the 44th IEEE Conference on Decision Control, 2005, pp. 6382–6387, https://doi.org/10.1109/CDC.2005.1583185.

[13] E. Iritani, *A review on modeling of pore-blocking behaviors of membranes during pressurized membrane filtration*, Dry. Technol., 31 (2013), pp. 146–162, https://doi.org/10.1080/07373937.2012.683123.

[14] J. Jimenez-Martinez and C. F. A. Negre, *Eigenvector centrality for geometric and topological characterization of porous media*, Phys. Rev. E, 96 (2017), 013310, https://doi.org/10.1103/PhysRevE.96.013310.

[15] R. O'Dea, J. J. Crofts, and M. Kaiser, *Spreading dynamics on spatially constrained complex brain networks*, J. R. Soc. Interface, 10 (2013), 20130016, https://doi.org/10.1098/rsif.2013.0016.

[16] M. Penrose, *Random Geometric Graphs*, Oxford University Press, New York, 2003.

[17] R. F. Probstein, *Physicochemical Hydrodynamics*, Wiley-Interscience, New York, 1994.

[18] P. Sanaei and L. J. Cummings, *Membrane filtration with complex branching pore morphology*, Phys. Rev. Fluids, 3 (2018), 094305, https://doi.org/10.1103/PhysRevFluids.3.094305.

[19] M. U. Siddiqui, A. F. Arif, and S. Bashmal, *Permeability-selectivity analysis of microfiltration and ultrafiltration membranes: Effect of pore size and shape distribution and membrane stretching*, Membranes, 6 (2016), 40, https://doi.org/10.3390/membranes6030040.

[20] W. Sun, T. Chen, C. Chen, and J. Li, *A study on membrane morphology by digital image processing*, J. Membr. Sci., 305 (2007), pp. 93–102, https://doi.org/10.1016/j.memsci.2007.07.040.

[21] G. Sundaramoorthi, M. Hadwiger, M. B. Romdhane, A. R. Behzad, R. Madhavan, and S. P. Nunes, *3D membrane imaging and porosity visualization*, Ind. Eng. Chem. Res., 55 (2016), pp. 3689–3695, https://doi.org/10.1021/acs.iecr.6b00387.

[22] R. Thiedmann, I. Manke, W. Lehnert, and V. Schmidt, *Random geometric graphs for modelling the pore space of fibre-based materials*, J. Mater. Sci., 46 (2011), pp. 7745–7759, https://doi.org/10.1007/s10853-011-5754-7.

[23] A. van der Schaft, S. Rao, and B. Jayawardhana, *On the mathematical structure of balanced chemical reaction networks governed by mass action kinetics*, SIAM J. Appl. Math., 73 (2013), pp. 953–973, https://doi.org/10.1137/11085431X.

[24] Z. Xie, Z. Ouyang, and J. Li, *A geometric graph model for coauthorship networks*, J Informetr., 10 (2016), pp. 299–311, https://doi.org/10.1016/j.joi.2016.02.001.

[25] W. Zhang, C. C. Lim, G. Korniss, and B. K. Szymanski, *Opinion dynamics and influencing on random geometric graphs*, Sci. Rep., 4 (2014), 5568, https://doi.org/10.1038/srep05568.